Correction of Sea Surface Wind Speed Based on SAR Rainfall Grade Classification Using Convolutional Neural Network

Chaogang Guo, Weihua Ai, Xi Zhang, Yanan Guan, Yin Liu, Shensen Hu, and Xianbin Zhao

***Abstract*—The technology of retrieving sea surface wind field from spaceborne synthetic aperture radar (SAR) is increasingly mature. However, the retrieval of the sea surface wind field related to the precipitation effect is still facing challenges, especially the strong precipitation related to extreme weather such as tropical cyclone will cause the wind speed retrieval error to exceed 10 m/s. Semantic segmentation and weak supervision methods have been used for SAR rainfall recognition, but rainfall segmentation is not accurate enough to support the correction of wind field retrieval. In this article, we propose to use deep learning to classify the rainfall grades in SAR images, and combine the rainfall correction model to improve the retrieval accuracy of sea surface wind speed. To overcome the challenge of limited training samples, the transfer learning method in fine-tune is adopted. Preliminary results demonstrate the effectiveness of this deep learning methodology. The model classifies rain and no-rain images with an accuracy of 96.2%, and classifies rainfall intensity grades with an accuracy of 86.2%. The rainfall correction model with SAR rainfall grade identified by convolution neural network reduces the root-mean-square error of retrieved wind speed from 3.83 to 1.76 m/s. The combination of SAR rainfall grade recognition and rainfall correction method improves the retrieval accuracy of SAR wind speed, which can further promote the operational application of SAR wind field.**

***Index Terms*—Convolutional neural network, correction, inception v3, rainfall, synthetic aperture radar (SAR), wind field.**

I. Introduction

SYNTHETIC aperture radar (SAR) with all-day, all-weather and high resolution is an important means to monitor the sea surface wind field. With the continuous updating of load and algorithm, the SAR based retrieval algorithm of sea surface wind field is gradually mature on the sea surface without rainfall. For example, National Oceanic and Atmospheric Administration (NOAA) used Sentinel-1 to launch the Alaska coastal SAR program [1]. The Canadian Space Agency used Radarsat-2 to launch the Canadian National SAR wind program [2]. However, it is still a challenge to overcome the effect of rainfall on the retrieval of sea surface wind field, especially the extreme weather such as tropical cyclones accompanied by heavy rainfall, which has a great effect on human life [3]. Although according to electromagnetic theory, atmospheric attenuation, and volume scattering caused by rainfall are more obvious in Ku band and can be almost ignored in C-band. However, it is more difficult to determine the scattering changes caused by the interaction of rainfall and sea surface in C-band [4]. The theoretical simulation research shows that when the rainfall intensity does not exceed 15 mm/h, the effect of rainfall on the normalized radar cross-section (NRCS) of vertical transmit/vertical receive (VV) polarization is mainly attenuation, which leads to the underestimate of wind speed. However, when the rainfall intensity exceeds 20 mm/h, the contribution of surface backscattering to effective NRCS is far less than the volume scattering of rainfall. Therefore, it is almost impossible to use NRCS to retrieve the surface wind vector under heavy rainfall conditions if the rainfall rate is not accurately understood [5]. The attenuation of scatterometer signal and volume backscattering by rainfall, as well as the disturbance of raindrops on the sea surface, indicate that rainfall is an important factor in SAR wind speed retrieval [6]. In the previous work, the scatterometer data showed that when the wind speed exceeds 30 m/s and the rainfall intensity exceeds 15 mm/h, the error of wind speed retrieval may exceed 10 m/s [7]. In addition, Reppucci et al. estimated the impact of heavy rain on C-band ocean backscattering based on the existing radiative transfer model. The results show that when the rainfall is 30 mm/h, the NRCS attenuation may exceed -1 dB. When the rainfall intensity exceeds 50 mm/h, the attenuation of NRCS will reach -2 dB [8].

Melsheimer et al. [9], [10] analyzed images of concurrent data of European Remote Sensing Satellite and weather stations, indicating that the C-band radar features of rain cells with rainfall rates below 50 mm/h comprised two main parts: volume scattering and attenuation of the SAR signals caused by raindrops and snow particles in the atmosphere, and an increase or decrease in the sea-surface roughness owing to the comprehensive effects of splashing raindrops. Retrieval of the sea-surface wind field is based on the empirical relationship

Manuscript received 26 October 2022; revised 3 November 2022; accepted 7 November 2022. Date of publication 24 November 2022; date of current version 7 December 2022. This work was supported in part by the Key Scientific Research Projects of Jiangsu Provincial Meteorological Bureau under Grant KZ202203 and in part by the fund of Key Laboratory of Atmosphere Sounding, CMA under Grant 2021KLAS01M. *(Corresponding author: Weihua Ai.)*

Chaogang Guo, Weihua Ai, Shensen Hu, and Xianbin Zhao are with the College of Meteorology and Oceanography, National University of Defense Technology, Changsha 410073, China (e-mail: a1137084323@163.com; awhzjax@126.com; hushensen18@nudt.edu.cn; zhaoxianbin@nudt.edu.cn).

Xi Zhang and Yanan Guan are with the First Institute of Oceanography, Ministry of Natural Resources, Qingdao 266061, China (e-mail: xi.zhang@fio.org.cn; b19010076@s.upc.edu.cn).

Yin Liu is with the Jiangsu Meteorological Observation Center, Key Laboratory of Atmosphere Sounding, Nanjing 210044, China (e-mail: liuyin200421@163.com).

Digital Object Identifier 10.1109/JSTARS.2022.3224438

between the sea-surface roughness and sea-surface wind speed, and changes in the sea-surface roughness are an important factor that affects the NRCS measured by SAR [11]. The empirical relationship between the NRCS and sea-surface wind speed was used to establish geophysical model functions (GMFs) between the VV polarization NRCS and sea-surface wind speed at low wind speeds [12] and between the vertical transmit/horizontal receive (VH) polarization NRCS and sea-surface wind speed at high wind speeds [13]. In the absence of rainfall, these GMFs can accurately retrieve the sea-surface wind field. Rainfall will affect the retrieval accuracy of GMFs. Especially in the complex environment of hurricane wind, rainfall will cause the wind speed error to reach 100% [14]. However, almost all existing GMFs do not include rainfall parameters or fully consider the effect of rainfall.

Correcting the effect of rainfall on SAR signals is very important for wind field retrieval. However, there is no instrument available on the SAR satellite platform to monitor rainfall synchronously. The high-resolution rainfall measurement provided by ground weather radar is limited to coastal areas, and its range is only a few hundred kilometers. Its detection height changes with the increase of the distance from the station, so it cannot provide accurate near ground rainfall rate. In places far from the coast, rainfall measurement mainly depends on satellite remote sensing [15]. The microwave radiometer SSMI/S can provide continuous observation covering almost half the earth, but its spatial resolution is low (8–14 km) [16].

Zhou et al. [17] used ASCAT scatterometer data and Tropical Rainfall Measuring Mission (TRMM) rainfall data to establish a C-band active microwave radiation transfer model under rainfall conditions, effectively improving the scatterometer wind field retrieval accuracy. Then, the rainfall of SAR observation time is calculated using geostationary IR images and nonsimultaneous passive microwave rainfall observation. Finally, the rainfall correction model is used to correct the SAR image, the corrected wind field is in good agreement with the NOAA Hurricane Research Division reanalysis data. Yu et al. [18] used Radarsat-2 data and quasi synchronous TRMM PR rainfall data to establish a fitting model of rain induced sea surface damped backscattering coefficient affected by rainfall intensity, incidence angle and other factors, which effectively improved the retrieval accuracy of SAR wind field under rainfall conditions.

Although the spaceborne SAR platform does not carry the precipitation measurement load at the same time, SAR can also capture rainfall and many other atmospheric and marine phenomena with its special imaging mode. In 1978, after the first ocean satellite SEASAT-A was launched, its L-band SAR captured rainfall [19]. In 1994, the space shuttle Endeavour carried the Spaceborne Imaging Radar-C/X-Band SAR (SIR-C/X-SAR) that was also used to capture rain cells. In SAR images, rain cells comprise bright and dark patches of irregular shapes, and the patch structure is closely related to the working frequency band and polarization mode of the radar [20]. Further developments of SAR have allowed the capture of radar features of rainfall in the C-band and X-bands. Analysis of SAR images has shown that heavy rainfall at sea increases the NRCS of the C-band and X-band and reduces the NRCS of the L-band [9].

The rainfall rate is an important parameter for analyzing the effect of rainfall on the SAR NRCS. However, the sea-surface wind field under rainfall conditions involves many physical processes of sea-air interactions. At present, no systematic theory has been established, and retrieving rainfall based on physical methods is still a challenge [18], [22]. Wang et al. [23] used convolutional neural network (CNN) to classify 10 geophysical phenomena including rainfall from SAR images. Colin et al. [24] realized semantic segmentation of ten oceanic processes in the context of a large quantity of image-level ground truths. Zhao et al. [25] used Sentinel-1 data and filters to realize automatic rainfall detection. Colin et al. [26] used Next Generation Weather Radar data and a CNN to segment the rainfall in SAR images with thresholds of 1, 3, and 10 mm/h. Incorporating ground reference data provides a reliable method for studying precipitation using SAR images. Lin et al. [27] estimated the rainfall rate according to the attenuation characteristics of NRCS in SAR images, and the results are consistent with the weather radar rainfall.

Since SAR cannot directly retrieve the rainfall rate, the current method of correcting the impact of rainfall on SAR signals is to use rainfall data of other loads, or use nonrainfall areas in SAR images to compare and analyze the impact of rainfall on SAR signals. But in fact, SAR and other loads can match in relatively few areas, and the coverage of meso and small-scale phenomena with the intensity reaching tropical cyclone is very large. The existing methods have limitations. The Sentinel-1 satellites of the European Space Agency (ESA) provide a large amount of reliable data for studying the interaction between the wind field and rainfall. The Global Precipitation Mission (GPM) dual-frequency precipitation radar (DPR) can provide the near-surface rainfall rate with a 5 km resolution as well as a vertical profile of the rainfall rate, and the minimum measurable rainfall rate is accurate to 0.2 mm/h, which is useful for rainfall research on using SAR. In this article, we propose to use deep learning to identify rainfall levels in SAR images, and combine existing rainfall correction models to correct wind speed retrieval of SAR images. The rest of this article is organized as follows. Section II introduces the data and products of the Sentinel-1 and GPM satellites as well as the data preprocessing. Section III introduces the CNN model and rainfall correction model. Section IV presents the results of the experiment and validation. Finally, Section V concludes this article.

II. Data and Preprocessing

A. Sentinel-1 Data and Preprocessing

Sentinel-1 is part of ESA's Copernicus program, and it is a dual constellation system comprising polar orbiting satellites A and B, which were launched on April 3, 2014 and April 25, 2016, respectively. Sentinel-1 operates in a near-polar solar synchronous orbit at an altitude of 679 km. Each of the two satellites carries a C-band SAR with a working frequency of 5.405 GHz. Each satellite has a revisit period of 12 days. Sentinel-1 was launched to provide observation data for research and applications in land, ocean, atmosphere, maritime search and rescue, and climate change [28].

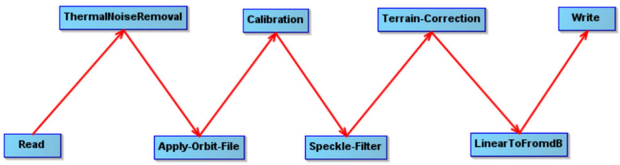

Fig. 1. Flowchart of Sentinel-1 IW data processing with SNAP.

Sentinel-1's SAR has four imaging modes: strip map, interferometric wide swath (IW), extra wide swath, and wave (WV). The core products of Sentinel-1 are provided at levels 0, 1, and 2. In this article, we used the VV polarization data of the level 1 ground range detected high-resolution product of IW mode. The resolution in range and azimuth is 20 m × 22 m and a cutting width of 250 km. This mode acquires three sub band images acquired by progressive terrain scanning that are then synthesized by corresponding algorithms [29]. This data is projected by multiview and World Geodetic System 84 projection on an ellipsoid model of earth. The pixel information indicated the detected amplitude, and the phase information was lost. The resolution of the generated product was almost the same in both directions, and speckle was reduced at the cost of reducing the spatial resolution.

The Sentinel Application Platform (SNAP) is software provided by the ESA for preprocessing Sentinel-1 data [30]. SNAP can process the data by creating a preprocessing flow chart, setting the processing and parameters required for the data, and directly entering the data can obtain the processed data. The flow chart of Sentinel-1 IW mode processing is shown in Fig. 1, including 8 steps. The image drawn by SAR VV NRCS is single channel, but the input of the Inception v3 model requires three channels of images. We fill the other two channels of the single channel image with single channel data.

B. Global Precipitation Mission Data and Products

The GPM satellite program is the successor to the TRMM. The core observation platform of GPM was launched on February 27, 2014, and it carried the GPM microwave imager and DPR. The DPR includes a Ku precipitation radar with a working frequency of 13.6 GHz and a Ka precipitation radar with a working frequency of 35.5 GHz. Its latitudinal coverage is 65°N–65° S, and it can detect weak precipitation and snowfall at a minimum rate of 0.2 mm/h [31]. GPM data products are divided into four levels, which are distributed by NASA Space Flight Center, and the 1–3 level products are public. In this article, we used data obtained by the normal scanning method of DPR products in the 6th edition. In this product, 49 points are scanned under the satellite at a time with a resolution of 5 km, scanning width of 245 km, and vertical resolution of 250 m.

C. Data Matching

To ensure that areas of different datasets were matched in the same time and space, we only retained data for which the difference between the GPM and SAR time tags did not exceed ±15 min. Fig. 2 shows a schematic diagram of the data matching.

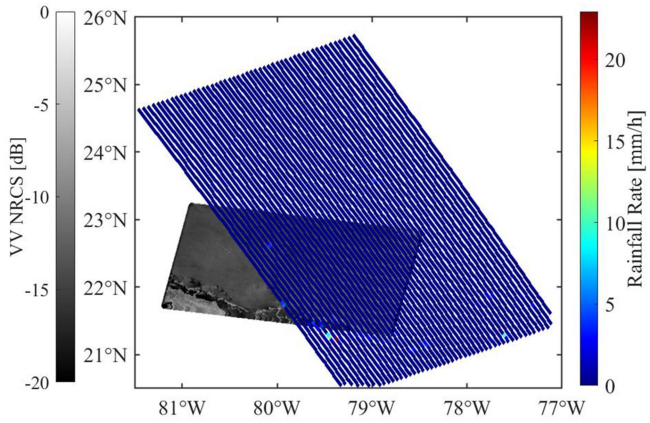

Fig. 2. Matching the areas of the GPM DPR (color) and Sentinel-1 (grayscale).

TABLE I
RAINFALL INTENSITY GRADES

Grade	Rainfall Intensity (mm/h)
Light Rain (LR)	0–2.5
Moderate Rain (MR)	2.5–8
Heavy Rain (HR)	8–16
Torrential Rain (TR)	≥16

The grayscale image shows the Sentinel-1 VV polarization NRCS, and the color image shows the GPM near-ground rainfall rate. To comply with the input requirements of the CNN and making the subimage resolution consistent with that of the GPM data, we cut the subimage to 224 pixels×224 pixels. Each subimage covered an area of 5 km × 5 km in the longitude and latitude directions.

D. Dataset

The GPM near-ground rainfall rate was used to obtain the initial labels of the subimages. As given in Table I, the data were divided into four rainfall intensity grades according to a meteorological standard [32]: light rain (LR), moderate rain (MR), heavy rain (HR), and torrential rain (TR). The standard considers the maximum rainfall rate for a rainstorm as 32 mm/h, but such instances were very scarce. Thus, we classified all rainfall rates greater than 16 mm/h as TR.

We matched Sentinel-1 and GPM data for the eastern Pacific and Atlantic Oceans from 2017 to 2018 and obtained 125 matches. Most of the matches were in the LR range, so few instances of data with rainfall intensities above LR were collected. We first built the dataset and only divided the subimages into two categories: rain and no rain (NR). This dataset was used to test whether the transfer-learning model could recognize rainfall in SAR images. Subsequently, we established a dataset that included NR and the four grades of rainfall intensity. For the first dataset, we set the number of subimages in the rain and NR

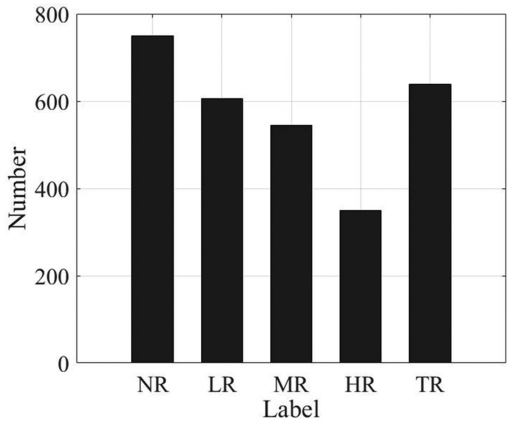

Fig. 3. Number of data types.

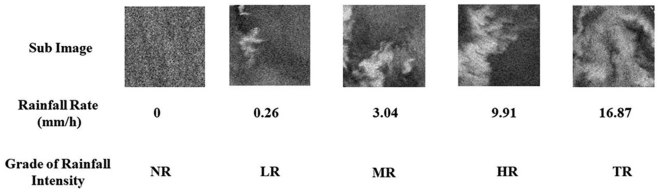

Fig. 4. Example subimages and corresponding rainfall intensity grades.

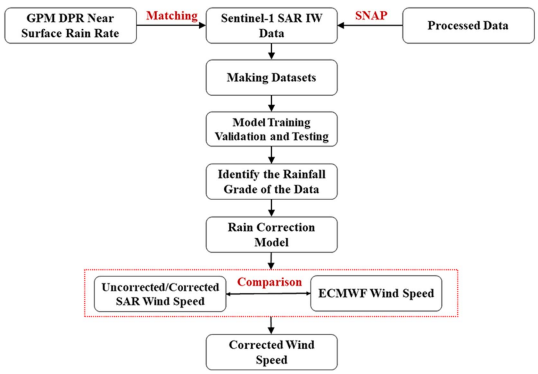

Fig. 5. Flow chart of wind field retrieval based on deep learning and rainfall correction mode.

categories to be consistent to avoid errors caused by the sample size. For the second dataset, Fig. 3 shows the number of data types. Examples of sub images of different rainfall grades are shown in Fig. 4. Both datasets were divided into a training set, validation set, and test set at a ratio of 7:2:1.

III. Rainfall Grade Identification and Wind Field Retrieval Correction

The flow chart of retrieving sea surface wind speed based on deep learning and rainfall correction model is shown in Fig. 5. First, match the data according to the time and space information of Sentinel-1 SAR and GPM DPR, and preprocess the matched SAR data using SNAP to obtain the calibrated NRCS (dB). Second, according to the input demand of the deep learning model and GPM DPR near surface rainfall rate, the rainfall grade dataset is made. Then, combining the rainfall grade recognized by the training model and the rainfall correction model, the NRCS of SAR images in the rain area is corrected. Finally, the Uncorrected/Corrected SAR wind speed and ECMWF wind speed are compared, and the correction model parameters are determined to obtain the corrected sea surface wind speed.

SAR images can capture a lot of atmospheric and marine phenomena, and dozens of sea surface phenomena have been recognized based on CNN. However, the number of collected sea surface phenomena is limited, and the new model is trained by means of transfer learning. In this article, the data that meets the time and space requirements of Sentinel-1 SAR and GPM DPR is even rarer, and it is still unable to establish a dataset with rich data, so transfer learning is also our best choice. Based on the radiative transfer model, several rainfall correction models related to rainfall rate have been established based on ASCAT, Radarsat-1, Radarsat-2 and Envisat SAR. After comparing these models, we choose the model with the best correction effect as the correction model for this article. Because the accurate rainfall rate cannot be obtained from SAR images, we input the intermediate value of the identified rainfall grade into the model for NRCS correction.

A. Convolutional Neural Network and Transfer Learning

The CNN concept was first proposed by LeCun. This neural network is good at extracting color, texture, and shape features of images, and it has obvious advantages for image processing. Inception Net is one of many CNN models [33], which was first used by Google in the ImageNet Large Scale Visual Recognition Challenge in 2014 [34]. Inception Net includes four types of models, and the Inception v3 model was adopted in this article. Inception v3 disassembles a large two-dimensional (2-D) convolution kernel into two smaller 1-D convolution kernels using the Inception v2 model and optimizes the structure of the Inception module. This method effectively reduces the number of model parameters, which suppresses overfitting and reduces the top-5 error rate from 4.8% to 3.5% [35].

The optimized Inception v3 is still a very deep network with a 48-layer network structure and more than 23 million network parameters [36]. Therefore, training a new Inception v3 model would require a large number of datasets, a long time, and high-performance hardware. However, we can use transfer learning to obtain the recognition function while avoiding this arduous process. The model is retrained by using the known dataset for application to small datasets. Wang et al. [23] used the Inception v3 model to classify geophysical phenomena in the Sentinel-1 WV data and achieved an overall accuracy of over 93% in 10 categories. Xia et al. [37] used Inception v3 and transfer learning to recognize nearly 20 kinds of flowers according to color, shape, and texture.

CNN is a multilevel deep structure, which is similar to other deep learning models. In the structure, many convolution layers are alternately distributed with pooling layers or subsampling layers, and at the end of the structure is one or more fully connected layers [38]. Its hierarchical structure helps to learn

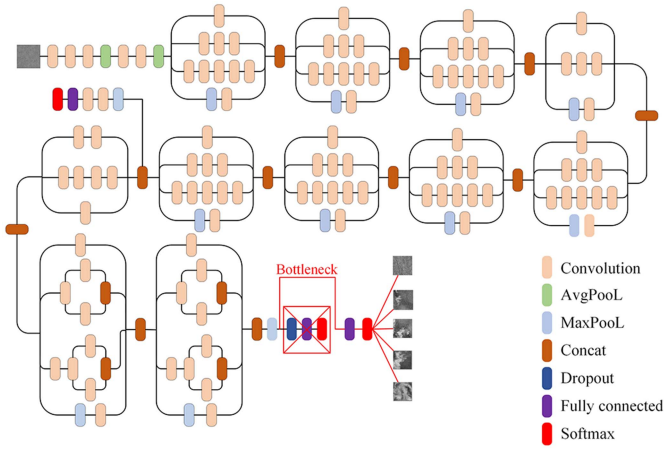

Fig. 6. Pretrained Inception v3 network structure (black connections) and the modified network structure (red connections).

invariant features and capture the hierarchical representation of features from low layers to high layers. The input is feedforward through two-stage convolution and subsampling operations to obtain the feature representation, and then the Gaussian classifier is used to generate the probability distribution [39]. For CNN, it usually contains three key components: convolution layer, pooling layer, and fully connected layer.

The function of the convolution layer is to extract different features of the input by using the convolution kernel. The distribution in the Inception v3 structure is shown in Fig. 6. Then, based on the nonlinear activation operation of the activation function, better eigenvalues are retained and scattered features are discarded. One of the most effective activation functions in the nonlinear activation layer is the rectification linear unit, which is a non-negative piecewise function that always obtains the maximum value between zero and input, as described in [40]

$$f(x) = \max(x, 0) = \begin{cases} x, x > 0 \\ 0, x \le 0 \end{cases}. \tag{1}$$

The role of pooling layer is to reduce the amount of network parameters and computation without losing image features. There are two common pooling methods: average pooling and maximum pooling. The most used is maximum pooling, which is generally better than average pooling. Pooling layer is mainly used to reduce the feature space dimension of CNN, but it will not reduce the deep. In addition, the pooling layer can effectively prevent the over fitting of the model and effectively improve the generalization ability of the model.

The full connection layer is at the network outlet, followed by the network output. Its function is mainly to complete the summary of eigenvalues and classify images according to the situation of eigenvalues. After fully extracting and compressing image features, the CNN will input all feature values to the full connection layer. The full connection layer will flatten the multidimensional feature map obtained in one dimension and then carry out activation operation. For object recognition, SoftMax classifier is commonly utilized to normalize the label probability, as mathematically described in [40]

$$\text{softmax}(y_i) = \frac{e^{y_i}}{\sum_{j=1}^{n} e^{y_i}}. \tag{2}$$

The research shows that Inception v3 model can well realize the recognition and classification of new images by changing the structure of the full connection layer and retaining the settings of all convolution layers. Transfer learning involves migrating the weights of a network pretrained on a large dataset to small datasets and then fine-tuning the network. The black connections part of Fig. 6 is a model trained by Imagenet dataset, which has 1000 categories and more than 1 million picture data. Then, we remove the last three layers of the original model, and input the feature output results of the original model to a new full connection for classification. The pretrained Inception v3 model has been successfully applied to extracting general features such as curves and edges of SAR images. In this article, we applied it to grading rainfall intensities. The default input image size of Inception-v3 is 299 pixels×299 pixels; however, the image size in the dataset was 224 pixels×224 pixels. We did not resize the images to 299 pixels×299 pixels when training and testing Inception-v3. This did not change the number of channels but instead changed only the size of the feature maps generated during the procedure, and the result was satisfactory.

B. Rainfall Correction Model

The effect of rainfall on SAR signals can be divided into three parts: the attenuation of rainfall on signals in the atmosphere, the volume scattering of raindrops in the atmosphere and the impact of raindrops on the sea surface, which change the sea surface roughness [6]. The rain-modified measured backscatter σ_m is

$$\sigma_m = (\sigma_{wind} + \sigma_{surf})\,\alpha_{atm} + \sigma_{atm} \tag{3}$$

where σ_m is the SAR-measured NRCS, σ_{wind} is the wind-induced surface backscatter predicted by the ECMWF and CMOD5, σ_{surf} is the rain-induced surface perturbation backscatter, α_{atm} is the two-way rain-induced atmospheric attenuation, and σ_{atm} is the rain-induced atmospheric backscatter. The net two-way atmospheric attenuation factor α_{atm} is expressed as

$$\alpha_{atm} = 10^{-0.2\int_0^H kdr} \tag{4}$$

where H is the height of melting layer, $k = 0.0031R$ is the atmospheric attenuation coefficient (dB/km) for 5.7 cm wavelength [17], where R is rain rate (mm/h). σ_{atm} is expressed as

$$\sigma_{atm} = \int_0^H 10^{-10}\frac{\pi^5}{\lambda^4}|K_w|^2 Z_e \cdot \alpha_{atm} dr \tag{5}$$

where λ is the wavelength (cm) of SAR; $K_w = (n^2-1)/(n^2+2)$ is a coefficient related to the absorption properties of water, which is assumed to be 0.93 for rain. $Z_e = 210R^{1.6}$ is the effective reflectivity (mm^6/m^3)) of the atmospheric rain. σ_{wind} is derived from (3)

$$\sigma_{\text{wind}} = \sigma_m\ \alpha_{atm}^{-1} - \sigma_{rain} \tag{6}$$

TABLE II
RELATION BETWEEN FITTED COEFFICIENTS AND INCIDENCE ANGLES AND RAINFALL INTENSITY FOR EQUATION (7)

Incidence angle (°)	p_0	p_1	p_2	p_3
27–33	1.00	2.86×10^{-4}	2.67×10^{-4}	3.74×10^{-5}
34–39	1.00	-2.47×10^{-4}	2.66×10^{-4}	5.27×10^{-5}
40–45	1.00	-6.38×10^{-5}	2.93×10^{-4}	5.21×10^{-5}
46–50	1.00	2.28×10^{-4}	3.31×10^{-4}	4.98×10^{-5}

TABLE III
RELATION BETWEEN FITTED COEFFICIENTS AND INCIDENCE ANGLES AND RAINFALL INTENSITY FOR EQUATION (8)

Incidence angle (°)	q_0	q_1	q_2	q_3
27–33	6.59×10^{-3}	-2.93×10^{-4}	1.47×10^{-5}	1.20×10^{-5}
34–39	2.61×10^{-3}	9.48×10^{-5}	2.43×10^{-5}	2.14×10^{-6}
40–45	1.91×10^{-3}	1.03×10^{-4}	3.31×10^{-5}	1.16×10^{-6}
46–50	1.56×10^{-3}	1.16×10^{-5}	1.65×10^{-5}	3.04×10^{-6}

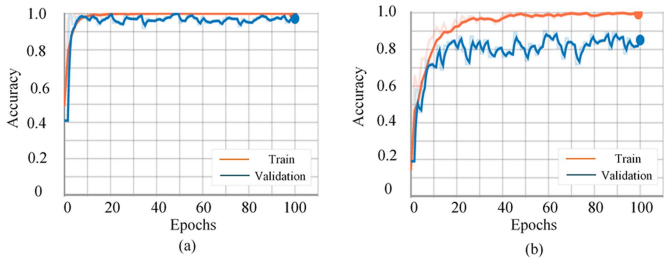

Fig. 7. Results of model training set (blue line) and validation set (red line). (a) Rain and NR dataset. (b) Dataset of different rainfall intensity grades.

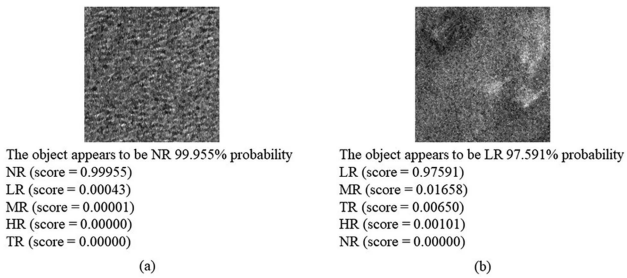

Fig. 8. Example recognition results using retrained models: (a) NR, (b) LR.

where $\sigma_{rain} = (\sigma_{atm}\alpha_{atm}^{-1} + \alpha_{surf})$, α_{atm}^{-1}, and σ_{rain} can be fitted with SAR data and rainfall rate

$$\alpha_{atm}^{-1}(\theta) = \sum_{n=0}^{3} p_n(\theta) R(\theta)^n \tag{7}$$

$$\sigma_{rain}(\theta) = \sum_{n=0}^{3} q_n(\theta) R(\theta)^n \tag{8}$$

where R is rainfall (dB·mm/h), p and q are fitting coefficients, and θ is the angle of incidence. The observation range of spaceborne SAR is about 15° to 50°. Considering that the incidence angle ranges of ASCAT and Sentinel-1 are similar, we use the coefficients fitted by the rainfall rates of ASCAT and TRMM. Table II shows the fitting coefficients of (7) with different incident angles. Table III shows the fitting coefficients of (8) with different incident angles.

IV. RESULTS AND VALIDATION

Fig. 7 shows the changes in the model accuracy over epochs with the training and validation sets. Fig. 7(a) shows the results with the rain and NR dataset. The accuracy tended to stabilize after 10 epochs with both the training and validation sets. The accuracy was close to 100% with the training set, about 98% with the validation set, and 96.2% with the test set. Fig. 7(b) shows the results with the dataset of different rainfall intensity grades. The accuracy increased rapidly with more epochs for both the training and validation sets. After 20 epochs, the trend slowed rapidly, and the accuracy fluctuated within a certain range. The model was trained for 30 epochs. The accuracy was mostly stable for the training set and fluctuated within a certain range for the validation set. The accuracy was about 99% for the training set, 85% for the validation set, and 86.2% for the test set.

Fig. 8 shows the recognition results of the rainfall intensity. Fig. 8(a) shows the NR recognition results, and Fig. 8(b) shows the LR recognition results. For each subimage, the first line gives the classification results of the model, and the second to sixth lines give the probability that the model would classify the subimage into a certain rainfall intensity grade.

Table IV presents the confusion matrix for the results with the test set. The retrained transfer-learning model was effective at recognizing NR and TR. Among LR subimages, 9.52% were wrongly classified as MR, and 4.76% were wrongly classified as NR. Among MR subimages, 6.66% were wrongly classified as LR, and 6.66% were wrongly classified as HR. Among HR subimages, 20% were wrongly classified as TR.

LR subimages may have been wrongly classified as NR if they lacked obvious features. The wrong classification of LR subimages as MR and MR subimages as LR and HR may be because the rainfall rate was at the threshold between these

TABLE IV
CONFUSION MATRIX OF THE CLASSIFICATION RESULTS USING THE MODEL

Actual \ Predicted	NR	LR	MR	HR	TR
NR	100.0%	0.00%	0.00%	0.00%	0.00%
LR	4.76%	85.71%	9.52%	0.0%	0.00%
MR	0.00%	6.660%	86.66%	6.66%	0.00%
HR	0.00%	0.00%	0.00%	80.00%	20.00%
TR	0.00%	0.00%	0.00%	0.00%	100%

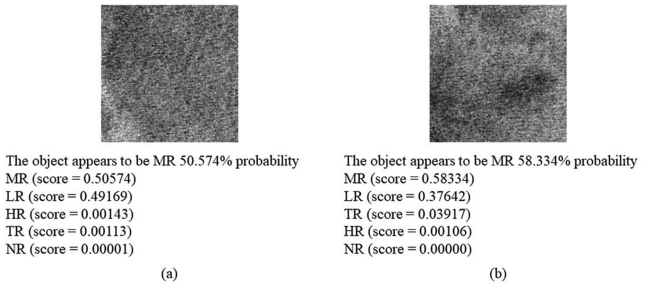

Fig. 9. LR subimages wrongly classified as MR.

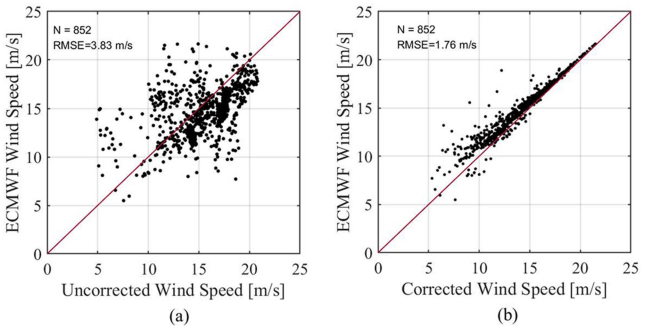

Fig. 10. Wind fields estimated from SAR versus reanalyzed data from ECMWF.

grades, and the differences between two adjacent grades were not particularly obvious. As shown in Fig. 9 shows two example LR subimages recognized as MR. The model assigned very similar probabilities to MR and LR. In addition, the rainfall ratios of these two subimages were 2.16 and 2.28 mm/h, respectively, which are very close to the threshold value of 2.5 mm/h between LR and MR. The wrong classification of HR subimages as TR was mainly because not enough HR data were collected, so the model was not sufficiently trained to extract HR features.

The Inception v3 model can only obtain the rainfall grade of SAR subimages, but not the accurate rainfall rate. Therefore, we input the intermediate values of all rainfall grades into the rainfall correction model. The comparison between the corrected SAR wind speed and the ECMWF wind speed is shown in Fig. 10. Fig. 10(a) contains the scatter plot of uncorrected SAR sea surface wind speed and ECMWF wind speed at all rainfall grades. The root-mean-square error of uncorrected rainfall affecting wind speed is 3.83 m/s. Fig. 10(b) shows the scatter plot of SAR sea surface wind speed and ECMWF wind speed after correction for the impact of rainfall. The root-mean-square error of the corrected wind speed is 1.76 m/s. It can be seen that the sea surface wind speed after rainfall correction is more consistent with the ECMWF wind speed.

V. CONCLUSION

Owing to the increasingly serious effects of climate change, monitoring the changes to extreme weather and meso- and small-scale phenomena in the oceans is of great importance to ensuring the safety of economic production and human lives. Conventional ground-based radar can only monitor land and offshore areas, so remote sensing is the main means of large-scale ocean monitoring. Although global wind-field and precipitation products are already available, there are still many challenges to improving the monitoring resolution and simultaneously monitoring the wind field and precipitation. Advances in SAR-related technology have led to the gradual application of SAR products to wind farms. Precipitation is an important factor that affects wind-field retrieval, but combining SAR and other loads is not practical. Therefore, we considered using deep learning to extract rainfall information from SAR images to eliminate their influence on wind-field retrieval.

In this article, we used the GPM near-surface rainfall rate as the reference data and labeled data according to the standard for rainfall intensity grades. We then used established datasets to train fine-tune a pretrained Inception v3 model. These results indicate that a CNN based on transfer learning can be used to recognize rainfall in SAR images. The model was then trained by using a dataset containing different rainfall intensities. The accuracy with the training and validation sets was lower than with the previous dataset containing only rain or NR but remained above 80%. These results are a preliminary confirmation that the rainfall intensity can be graded according to features captured by SAR images. However, at present, there are not many Sentinel-1 data and GPM near surface precipitation data that can be matched, leading to the recognition effect of the retrained model around some rainfall level threshold still needs to be further improved. Finally, it is verified that the median value of rainfall grade identified by CNN is input into the existing rainfall correction model, which can effectively reduce the impact of rainfall on wind field retrieval. However, the modified correction model is more suitable for the area with higher wind speed, and it needs to be improved or fitted with a new model in the area with lower wind speed.

Our next step is to match more Sentinel-1 and GPM DPR data. On the one hand, it is to further improve the generalization rate and classification accuracy of the model. On the other hand, it is to fit a rainfall correction model based on Sentinel-1 and GPM DPR near ground rainfall rate, so as to realize automatic recognition of SAR rainfall phenomena and wind field correction. Retrieval of the sea-surface wind field based on remote sensing is a relatively mature technology for conventional applications, but the interaction between the sea-surface wind field and precipitation has not yet been established as a complete physical model. If more rainfall and wind information can be obtained from SAR images at the same time, it will be helpful to this part of the article.

REFERENCES

[1] C. R. J. Monaldo, W. G. Pichel, and X. Li, "A weather eye on coastal winds," *Eos Trans. Amer. Geophysical Union*, vol. 96, no. 17, pp. 16–19, 2015.

[2] S. Khurshid, D. Bradley, M. Manore, and C. Fogarty, "National SAR winds project," in *Proc. 33rd Can. Symp. Remote Sens.*, 2012, pp. 1–2.

[3] D. E. Weissman et al., "Challenges to satellite sensors of ocean winds: Addressing precipitation effects," *J. Atmospheric Ocean. Technol.*, vol. 29, no. 3, pp. 356–374, Mar. 2012.

[4] B. W. Stiles and R. S. Dunbar, "A neural network technique for improving the accuracy of scatterometer winds in rainy conditions," *IEEE Trans. Geosci. Remote Sens.*, vol. 48, no. 8, pp. 3114–3122, Aug. 2010.

[5] J. Tournadre and Y. Quilfen, "Impact of rain cell on scatterometer data: 1. Theory and modeling," *J. Geophysical Res.*, vol. 108, no. 7, 2003, Art. no. 18, doi: 10.1029/2002jc001428.

[6] C. Nie and D. G. Long, "A C-band wind/rain backscatter model," *IEEE Trans. Geosci. Remote Sens.*, vol. 45, no. 3, pp. 621–631, Mar. 2007.

[7] J. Yang, X. Zhang, X. Chen, Y. Ke, and F. Marks, "Effect of precipitation on ocean wind scatterometry," in *Proc. IEEE Int. Geosci. Remote Sens. Symp.*, 2004, pp. 4913–4916.

[8] A. Reppucci, S. Lehner, J. Schulz-Stellenfleth, and C. S. Yang, "Extreme wind conditions observed by satellite synthetic aperture radar in the North West Pacific," *Int. J. Remote Sens.*, vol. 29, no. 21, pp. 6129–6144, 2008.

[9] C. Melsheimer, W. Alpers, and M. Gade, "Investigation of multifrequency/multipolarization radar signatures of rain cells over the ocean using SIR-C/X-SAR data," *J. Geophysical Res., Oceans*, vol. 103, no. C9, pp. 18867–18884, 1998.

[10] C. Melsheimer, W. Alpers, and M. Gade, "Simultaneous observations of rain cells over the ocean by the synthetic aperture radar aboard the ERS satellites and by surface-based weather radars," *J. Geophysical Res. Oceans*, vol. 106, no. C3, pp. 4665–4677, 2001.

[11] J. Horstmann, H. Schiller, J. Schulz-Stellenfleth, and S. Lehner, "Global wind speed retrieval from SAR," *IEEE Trans. Geosci. Remote Sens.*, vol. 41, no. 10, pp. 2277–2286, Oct. 2003, doi: 10.1109/tgrs.2003.814658.

[12] S. Lehner, W. Rosenthal, and W. Koch, "Mesoscale wind measurements using recalibrated ERS SAR images," in *Proc. 3rd IFREMER Workshop IRS Wind Wave Meas.*, 1996, Art. no. 1996.

[13] H. Shen, W. Perrie, Y. J. He, and G. Q. Liu, "Wind speed retrieval from VH dual-polarization RADARSAT-2 SAR images," *IEEE Trans. Geosci. Remote Sens.*, vol. 52, no. 9, pp. 5820–5826, Sep. 2014, doi: 10.1109/tgrs.2013.2293143.

[14] R. Moore, A. Chaudhry, and I. Birrer, "Errors in scatterometer-radiometer wind measurement due to rain," *IEEE J. Ocean. Eng.*, vol. 8, no. 1, pp. 37–49, Jan. 1983, doi: 10.1109/JOE.1983.1145541.

[15] G. Liu, "Satellite remote sensing | precipitation," *Encyclopedia Atmospheric Sci.*, J. R. Holton Ed. Oxford: Academic Press, pp. 1972–1979, 2003.

[16] E. A. Smith, G. Asrar, Y. Furuhama, A. Ginati, and W. Zhang, *International Global Precipitation Measurement (GPM) Program and Mission: An Overview*. Amsterdam, The Netherlands: Springer, 2007.

[17] X. Zhou et al., "Estimation of tropical cyclone parameters and wind fields from SAR images," *Sci. China-Earth Sci.*, vol. 56, no. 11, pp. 1977–1987, 2013.

[18] Y. Shui et al., "The correction of rain effect on SAR wind field retrieval," *Haiyang Xuebao*, vol. 39, no. 9, pp. 40–50, 2017.

[19] L. L. Fu and B. Holt, "SEASAT views oceans and sea ice with synthetic aperture radar," *JPL Publ.*, vol. 81-120, Mar. 1982.

[20] D. Atlas, "Origin of storm footprints on the sea seen by SAR," in *Proc. IEEE Int. Geosci. Remote Sens. Symp.*, 1994, Art. no. 1776.

[21] C. Melsheimer, W. Alpers, and M. Gade, "Investigation of multifrequency/multipolarization radar signatures of rain cells over the ocean using SIR-C/X-SAR data," *J. Geophysical Res., Oceans*, vol. 103, no. C9, pp. 18867–18884, 1998.

[22] J. Shi, J. Hu, W. Shao, X. Wang, and X. Li, "The impact of rain to observed signal from Chinese Gaofen-3 synthetic aperture radar in typhoons," *Acta Oceanologica Sinica*, vol. 38, no. 11, pp. 121–133, 2019.

[23] C. Wang et al., "Automated geophysical classification of sentinel-1 wave mode SAR images through deep-learning," in *Proc. IEEE Int. Geosci. Remote Sens. Symp.*, 2018, pp. 1776–1779.

[24] A. Colin et al., "Semantic segmentation of metoceanic processes using SAR observations and deep learning," *Remote Sens.*, vol. 14, no. 4, 2022, Art. no. 851.

[25] Y. Zhao, N. Longépé, A. Mouche, and R. Husson, "Automated rain detection by dual-polarization sentinel-1 data," *Remote Sens.*, vol. 13, no. 16, 2021, Art. no. 3155.

[26] A. Colin, P. Tandeo, C. Peureux, R. Husson, N. Longepe, and R. Fablet, "Rain rate estimation with SAR using NEXRAD measurements with convolutional neural networks," *Comput. Sci.*, 2022, *arXiv:2207.07333*.

[27] I. Lin, D. Kasilingam, W. Alpers, T. K. Lim, H. Lim, and V. Khoo, "A quantitative study of tropical rain cells from ERS SAR imagery," in *Proc. IEEE Int. Geosci. Remote Sens. Symp.*, 1997, pp. 1527–1529.

[28] D. Geudtner, R. Torres, P. Snoeij, D. Bibby, and B. Rommen, "Sentinel-1 system," in *Proc. EUSAR 10th Eur. Conf. Synthetic Aperture Radar*, 2014, pp. 1–3.

[29] N. Miranda, B. Rosich, and C. Putignano, "The Sentinel-1 data processor and operational products," in *Proc. IEEE Int. Geosci. Remote Sens. Symp.*, 2012, pp. 1730–1733, doi: 10.1109/igarss.2012.6351188.

[30] F. Filipponi, "Sentinel-1 GRD preprocessing workflow," *Proceedings*, vol. 18, no. 1, 2019, Art. no. 11.

[31] G. Tang et al., "An overview of the global precipitation measurement (GPM) mission and it's latest development," *Remote Sens. Technol. Appl.*, vol. 4, pp. 607–615, 2015.

[32] L. Tian, Y.-J. Zeng, and X. Fu, "Velocity ratio of wind-driven rain and its application on a transmission tower subjected to wind and rain loads," *J. Perform. Constructed Facilities*, vol. 32, no. 5, Oct. 2018, Art. no. 04018065.

[33] R. Usha and K. Perumal, "Content based image retrieval using combined features of color and texture features with SVM classification," *Comput. Sci.*, 2014.

[34] M. Z. Alom, T. M. Taha, C. Yakopcic, S. Westberg, and V. K. Asari, "The history began from AlexNet: A comprehensive survey on deep learning approaches," *Comput. Sci.*, 2018, *arXiv:1803.01164*.

[35] C. Szegedy, V. Vanhoucke, S. Ioffe, J. Shlens, and Z. Wojna, "Rethinking the inception architecture for computer vision," in *Proc. IEEE Conf. Comput. Vis. Pattern Recognit.*, 2016, pp. 2818–2826.

[36] O. Albatayneh, L. Forslöf, and K. Ksaibati, "Image retraining using TensorFlow implementation of the pretrained inception-v3 model for evaluating gravel road dust," *J. Infrastructure Syst.*, vol. 26, no. 2, 2020, Art. no. 04020014.

[37] X. L. Xia, C. Xu, and B. Nan, "Inception-v3 for flower classification," in *Proc. 2nd Int. Conf. Image Vis. Comput.*, 2017, pp. 783–787.

[38] Y. LeCun, Y. Bengio, and G. Hinton, "Deep learning," *Nature*, vol. 521, no. 7553, pp. 436–444, May 2015, doi: 10.1038/nature14539.

[39] Y. Lecun et al., "Backpropagation applied to handwritten zip code recognition," *Neural Computation*, vol. 1, no. 4, pp. 541–551, 1989.

[40] L. Chunmian, L. Lin, L. Wenting, K. C. P. Wang, and G. Jiangang, "Transfer learning based traffic sign recognition using inception-v3 model," *Periodica Polytechnica, Transp. Eng.*, vol. 47, no. 3, pp. 242–250, 2019, doi: 10.3311/PPtr.11480.